
Generic Orthogonal Moments and Applications

C. Camacho-Bello, C. Toxqui-Quitl and A. Padilla-Vivanco

We present a detailed analysis of the Jacobi-Fourier moments and their applications in digital image processing. In order to reach numerical stability during the computation of the Jacobi radial polynomials a recursive approach is described. Also, some discussions are done about the best values of the parameters α and β in terms of its performance. Moreover, the digital image applications studied here are divided in low or high orders n of the polynomials. Typically, the pattern recognition applications are based in low order polynomials whilst image reconstruction can be achieved by using high order polynomials. On the other hand, the polar pixel approach is taken into account, in order to increase the numerical accuracy in the calculation of the

C. Camacho-Bello
Universidad Politécnica de Tulancingo, Calle Ingenierías No. 100, 43629, Hidalgo, México
Instituto Nacional de Astrofísica, Óptica y Electrónica,
Calle Luis Enrique Erro No. 1, 72840, Puebla, México
e-mail: joel_camacho@inaoep.mx

C. Toxqui-Quitl, A. Padilla-Vivanco
Universidad Politécnica de Tulancingo, Calle Ingenierías No. 100, 43629, Hidalgo, México
e-mail: carina.toxqui@upt.edu.mx, alfonso.padilla@upt.edu.mx

moments, also some ad hoc cases using this polar geometry are studied. Experiments and results are presented.

8.1 Introduction

The circular orthogonal moments are widely used in pattern recognition, image analysis and computer vision. They have the ability to characterize, evaluate, and manipulate digital information with minimum redundant information. Teague [17] was the first who introduced the notion of circular orthogonal moments over the basis set of the *Zernike polynomials*. He used a kernel composed of a radial orthogonal polynomial and an angular Fourier complex function. Bhatia and Wolf [3] pointed out that there is an infinite number of complete sets of radial orthogonal polynomials which can be obtained from the Jacobi polynomials. The variation of parameters α and β of the Jacobi polynomials can produce different sets of known orthogonal moments [7, 12], such as *orthogonal Fourier–Mellin moments* [14] ($\alpha = \beta = 2$), *Chebyshev–Fourier moments* [13] ($\alpha = 2, \beta = 3/2$), *Pseudo-Jacobi–Fourier moments* [2] ($\alpha = 4, \beta = 3$), *Legendre–Fourier Moments* ($\alpha = \beta = 1$), *Zernike* [17] ($J_s(m+1, m+1, r^2)$) and *Pseudo-Zernike Moments* [18] ($J_s(2m+2, m+2, r), n = m+s$).

Ping et al. [12] appoints the *Jacobi–Fourier moments* as *Generic orthogonal moments* and suggested that the common formulation of the orthogonal moments through the Jacobi polynomials will be an advantage for performance analysis of the orthogonal moments; and for searching a prime orthogonal moment. This last idea has been ignored due to its high computational costs.

The wide range of applications of the Jacobi–Fourier moments have been explored in different contexts [20], [10], [5]. In all of these investigations, various questions of interest have emerged: 1) how find the best selection from the infinity of possibilities for α and β parameters; and therefore to determine the radial polynomial set according to the particular application, 2) how to correct the numerical instability of high order radial polynomials for values close to $r = 1$, and 3) how to beat down the classical geometric error between the grid of pixels in digital images and the unit disk where the polynomials are defined.

This chapter presents a review of the Generic orthogonal moments and some of their applications in the digital image processing areas. Some criteria are implemented to narrow the number of possibilities for the parameters α and β in the pattern recognition cases that are presented here. Also for obtaining a good combination of the radial and angular orders a descriptor map is proposed and evolved by using Genetic algorithms. Two specific applications of pattern recognition are analysed: a) human gait recognition and b) mechanical parts recognition including the case of motion-blurred images. Another interesting application of the use of Jacobi–Fourier moments is found in Multifocus image fusion from optical microscope images. The analysis is done based on a classical fusion scheme of blocks. The Jacobi–Fourier moments are used as a focus measure for evaluating the contrast or sharpness of each image block. The results are presented for RGB images.

In relation with the square-circular symmetry drawback between digital images and unit disk, a comparative analysis in terms of the image reconstruction error with the

arrangement of polar pixels is presented. For works [5] and [23], only conducted tests have been performed using the test images such as Lena and the boat, but not for images with radial symmetry that may have some medical application, such as iris and retina or for Ronchigram images which are widely used in optical testing. Additionally, the analysis aims to understand the ability to characterize an image depending on its shape in order to determine the parameters α and β , which are the best suited to specific applications. Furthermore, this chapter compares the implementation of the radial Jacobi polynomials by use of the recursive relationships against the generic radial formula.

Our exposition is organized as follows: Section 8.2 presents an overall review of the Generic Jacobi- Fourier moments of an image based on Jacobi-Fourier polynomials. This review includes the recurrence relationships for its computation. In Section 8.3 an application in the area of pattern recognition, the classification of mechanical parts and blurred-motion objects, is analyzed. In Section 8.4, a detailed analysis based on the Jacobi-Fourier moment histories of the human gait is presented. In Section 8.5, a multifocus fusion method for color images is implemented, in order to evaluate the effectiveness of the Jacobi-Fourier moments in combination with a multi-sensor image fusion scheme. Section 8.6 is related to the new approach of polar pixels and its mathematical review, also shows the mapping of some images from square to polar pixels. Three interesting cases of image reconstructions using the methods studied in this chapter are described in Section 8.7. Finally, in Section 8.8 the conclusions of our research are presented.

8.2 Generic Jacobi Fourier Moments

The general expression for JFMs of order n and repetition m , for a given image function $f(r, \theta)$ in polar coordinates is given by

$$\phi_{n,m} = \int_0^{2\pi} \int_0^1 f(r, \theta) P_{n,m}(r, \theta) r dr d\theta, \quad (8.1)$$

where $P_{n,m}(r, \theta)$ is the kernel function that consists of two separable functions sets: the Jacobi orthogonal polynomial $J_n(\alpha, \beta, r)$ and exponential Fourier factor $\exp(jm\theta)$, expressed by

$$P_{n,m}(r, \theta) = J_n(\alpha, \beta, r) \exp(jm\theta). \quad (8.2)$$

For digital images, the Eq.(8.1) cannot be directly applied. Let $f(r_{i,j}, \theta_{i,j})$ be a digital image with spatial dimensions $M \times N$. Its discrete moments $\phi_{n,m}$ are given by

$$\tilde{\phi}_{n,m} = \sum_{i=0}^{M-1} \sum_{j=0}^{N-1} f(r_{i,j}, \theta_{i,j}) \tilde{P}_{nm}(r_{i,j}, \theta_{i,j}) \quad (8.3)$$

where the discrete polar coordinates are expressed by

$$r_{i,j} = \sqrt{x_i^2 + y_j^2} \quad r_{i,j} \leq 1, \quad (8.4)$$

$$\theta_{i,j} = \arctan\left(\frac{y_j}{x_i}\right), \quad (8.5)$$

and they are transformed by

$$x_i = -1 + \frac{2i}{N-1}, \quad y_j = -1 + \frac{2j}{M-1} \quad (8.6)$$

where $i = 0, \dots, N-1$, and $j = 0, \dots, M-1$. When the integrals of Eq.(8.1) are replaced by summations and the image is normalized inside the unit disk, this approach is known as zeroth-order approximation or direct method.

Ping et al. [12] first used the shifted orthonormal Jacobi polynomials as kernel for circular moments, which are defined as follows

$$J_n(\alpha, \beta, r) = \sqrt{\frac{w(\alpha, \beta, r)}{b_n(\alpha, \beta) r}} G_n(\alpha, \beta, r) \quad (8.7)$$

where $G_n(\alpha, \beta, r)$ are the Jacobi polynomials, $b_n(\alpha, \beta)$ is the normalization constant, and $w(\alpha, \beta, r)$ is the weight function [1]. These expressions are computed as follows [7],

$$G_n(\alpha, \beta, r) = \frac{n! \Gamma(\beta)}{\Gamma(\alpha+n)} \times \sum_{s=0}^n (-1)^s \frac{\Gamma(\alpha+n+s)}{(n-s)! s! \Gamma(\beta+s)} r^s, \quad (8.8)$$

$$b_n(\alpha, \beta) = \frac{n! \Gamma^2(\beta) \Gamma(\alpha - \beta + n + 1)}{\Gamma(\beta+n) \Gamma(\alpha+n) (\alpha+2n)}, \quad (8.9)$$

$$w(\alpha, \beta, r) = (1-r)^{\alpha-\beta} r^{\beta-1} \quad (8.10)$$

where $\Gamma(\cdot)$ is the Gamma function, $\alpha - \beta > -1$ and $\beta, \alpha > 0$. The radial function $J_n(r)$ satisfies the orthogonality property given by,

$$\int_0^1 J_n(\alpha, \beta, r) J_k(\alpha, \beta, r) r dr = \delta_{nk}, \quad (8.11)$$

where δ_{nk} is the Kronecker symbol. The calculations of factorials and gamma function in Eq.(8.8) and Eq.(8.9) increases the computation time and they are only accurate for factorials less than 21. Moreover, the computation of the n th power of r in higher orders than 21 cause numerical instability in values around $r = 1$ inside the unit disc. Recently, Camacho et al. [5] proposed a recurrence relation with respect to n to increase the numerical stability for the computation of the shifted Jacobi polynomials. The recursive relation is given by

$$A_n J_n(\alpha, \beta, r) = (2r - 1 - B_n) J_{n-1}(\alpha, \beta, r) - A_{n-1} J_{n-2}(\alpha, \beta, r), \quad (8.12)$$

where $r \in [0, 1]$, $\alpha - \beta > -1$, $\beta, \alpha > 0$ and the coefficients A_n and B_n are computed as follows

$$A_n = \sqrt{\frac{4n(n + \alpha - \beta)(n + \beta - 1)(n + \alpha - 1)}{(2n + \alpha - 1)^2(2n + \alpha)(2n + \alpha - 2)}}, \quad (8.13)$$

$$B_n = \frac{(\alpha - 1)(2\beta - \alpha - 1)}{(2n + \alpha - 1)(2(n - 1) + \alpha - 1)}. \quad (8.14)$$

To start with the numerical computation, the Jacobi polynomials of zero and first normalized orders are given by

$$J_0(\alpha, \beta, r) = \sqrt{\frac{w(\alpha, \beta, r)}{b_0(\alpha, \beta)}}, \quad (8.15)$$

$$J_1(\alpha, \beta, r) = J_0(\alpha, \beta, r) \sqrt{\frac{(\alpha + 2)\beta}{\alpha - \beta + 1}} \left(\frac{\alpha + 1}{\beta} r - 1 \right). \quad (8.16)$$

Figure 8.1 shows how the numerical instability from Eq.(8.7) grows when the order increases contrary to the recurrence relation of Eq.(8.12), which is much more stable. On the other hand, changing the parameters α and β in the recurrence relationships, it is possible to generate different families of known orthogonal polynomials with less computation time. Some cases of these polynomial families with their recurrence relationships are shown in Table 8.1. Moreover, the first six orders of the radial polynomials are shown in Fig.(8.2).

8.3 Pattern Recognition

This section provides some examples, where the theory of generic orthogonal moments has applicability. Since the moments are image invariant descriptors, the most common use is in the pattern recognition areas. Also, they have been used in image enhancement applications. In the first part of this section, we present an analysis of the use of low order moments in the context of object classification, biometrics and later their effectiveness in the evaluation of multifocus image fusion.

8.3.1 Object Classification

In every industrial production line, the control of shape, size and quality is an important task. Currently, manual inspection is not implemented because of being expensive, time consuming, and often inaccurate. Contrary, the automatic inspection is inexpensive and time efficient, and can be used both to remove defective objects from the production line and to grade objects according to size, shape, and quality. In order to control the quality of manufactured products such as mechanical parts, many computational techniques have been proposed into the automatic inspection process [4][6]. In the case of the production of mechanical parts in hostile industrial conditions, such

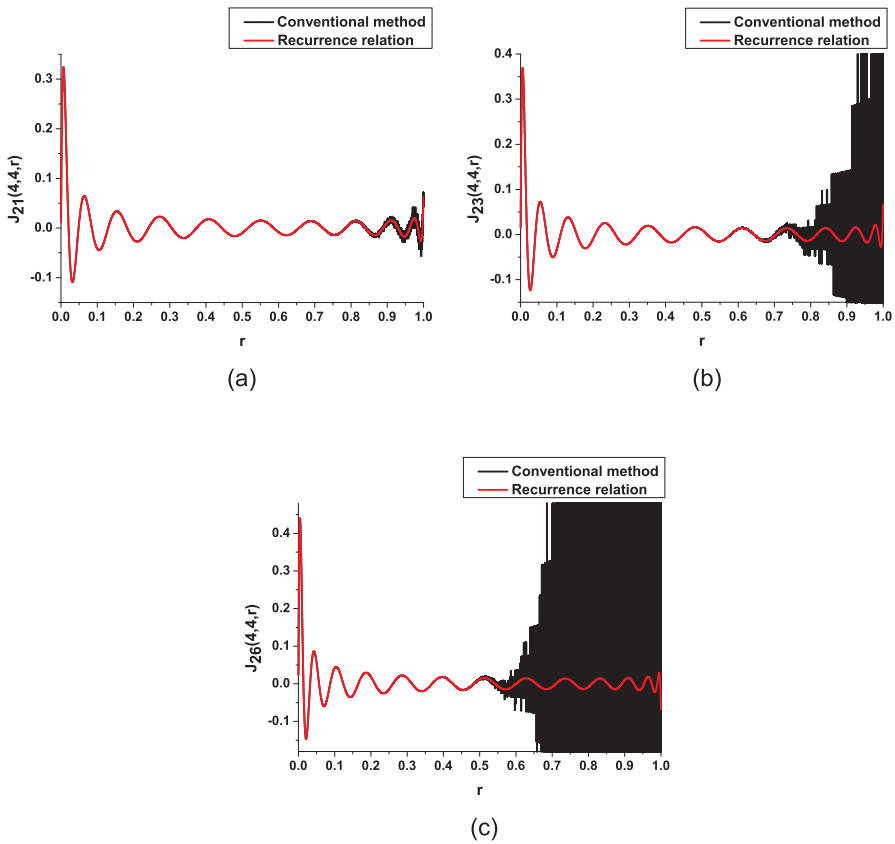


Figure 8.1: Numerical instability correction of Jacobi polynomials when $\alpha = \beta = 4$ for the orders: (a) $n = 21$, (b) $n = 23$, and (c) $n = 26$.

Table 8.1: Parameters of the recurrence relation for different known polynomials

Radial orthogonal polynomial	Coefficients	Polynomials of zero and first orders
<p>Legendre</p> <p>$L_n(r) = J_n(1, 1, r)$</p>	<p>$A_n = \frac{n}{\sqrt{4n^2-1}}$</p> <p>$B_n = 0$</p>	<p>$L_0(r) = \frac{1}{\sqrt{r}}$</p> <p>$L_1(r) = L_0(r) \sqrt{3}(2r - 1)$</p>
<p>Chebyshev</p> <p>$C_n(r) = J_n(2, 3/2, r)$</p>	<p>$A_n = \frac{1}{2}$</p> <p>$B_n = 0$</p>	<p>$C_0(r) = \sqrt{\frac{8}{\pi}} \left(\frac{1-r}{r}\right)^{\frac{1}{4}}$</p> <p>$C_1(r) = C_0(r)(4r - 2)$</p>
<p>Pseudo-Jacobi</p> <p>$P_n(r) = J_n(4, 3, r)$</p>	<p>$A_n = \frac{2n+3}{\sqrt{n(n+3)}}$</p> <p>$B_n = \frac{3}{4n^2-1}$</p>	<p>$P_0(r) = \sqrt{r(1-r)} 12$</p> <p>$P_1(r) = P_0(r) \sqrt{9} \left(\frac{3}{5}r - 1\right)$</p>
<p>Mellin</p> <p>$M_n(r) = J_n(2, 2, r)$</p>	<p>$A_n = \frac{\sqrt{n(n-1)}}{2n+1}$</p> <p>$B_n = \frac{1}{4n^2-1}$</p>	<p>$M_0(r) = \sqrt{2}$</p> <p>$M_1(r) = 6r - 2$</p>
<p>Zernike</p> <p>$Z_n^m(r) = J_s(m+1, m+1, r^2)$</p> <p>$n = 2s + m$</p>	<p>$A_n = \frac{(n-m)(n+m)}{2n\sqrt{(n+1)(n-1)}}$</p> <p>$B_n = \frac{m^2}{n(n-2)}$</p>	<p>$Z_m^m(r) = \begin{cases} \sqrt{2(m+1)}r^m & m \neq 0 \\ \sqrt{(m+1)}r^m & m = 0 \end{cases}$</p> <p>$Z_{m+2}^m(r) = Z_m^m(r) \sqrt{(m+3)(m+1)} \times \left(\frac{m+2}{m+1}r^2 - 1\right)$</p>
<p>Pseudo-Zernike</p> <p>$PZ_n^m(r) = J_s(2m+2, 2m+2, r)$</p> <p>$n = s + m$</p>	<p>$A_n = \frac{(n-m)(n+m+1)}{(2n+1)\sqrt{(n+1)n}}$</p> <p>$B_n = \frac{(2m+1)^2}{4n^2-1}$</p>	<p>$PZ_m^m(r) = \sqrt{2(m+1)}r^m$</p> <p>$PZ_{m+1}^m(r) = PZ_m^m(r) \sqrt{(m+2)(m+1)} \times \left(\frac{2m+3}{m+1}r - 2\right)$</p>

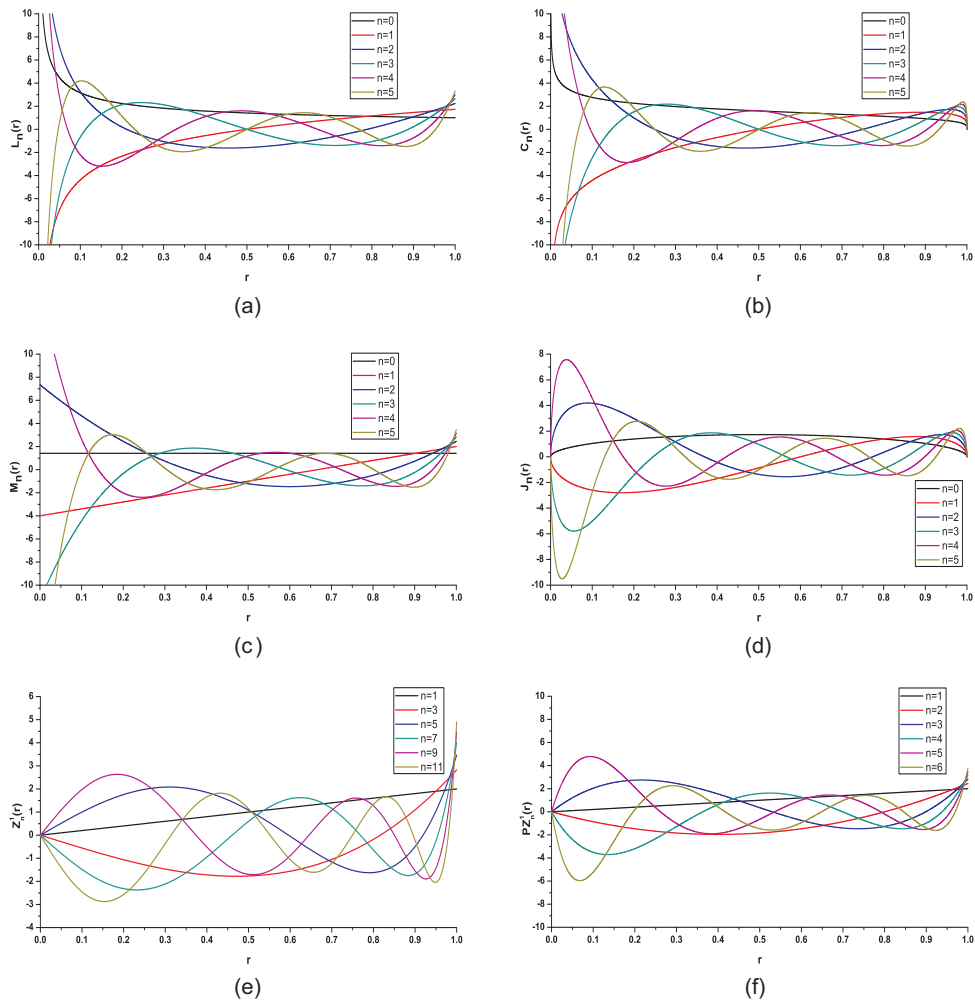


Figure 8.2: First six orders of radial polynomials. (a) Legendre, (b) Chebyshev, (c) Mellin, (d) Pseudo Jacobi, (e) Zernike, and (f) Pseudo-Zernike.



Figure 8.3: Some training images.

as high vibrations or rotations from internal or external vibration sources to the production line, the quality control is commonly affected by these kinds of motions. To overcome these drawbacks the method of moments can be well addressed to grade multidistorted images which have been smeared by motion.

The invariant JFMs are given by,

$$\tilde{\phi}_{n,m} = gc^2 \left| \sum_{i=0}^{M-1} \sum_{j=0}^{N-1} f_d(r_{i,j}, \theta_{i,j}) \tilde{P}_{nm}(r_{i,j}, \theta_{i,j}) \right| \quad (8.17)$$

where $f_d\left(\frac{r_{i,j}}{c}, \theta_{i,j}\right)$ is a spatial transformed image by a scale factor c and with an intensity change g . As the circular moments are not shift, scale, and intensity change invariant in themselves, the non orthogonal Geometric central moments $\mu_{pq}^f = \sum_{i=0}^{M-1} \sum_{j=0}^{N-1} f(i, j) (i - cx)^p (j - cy)^q$ are used to normalize them. From this point view, the scale factor and centroid position of the object in the image can be obtained, respectively, by $c = \sqrt{\frac{\mu_{00}^f}{\mu_{00}^{referencia}}}$ and $\left[cx = \frac{m_{10}}{m_{00}}, cy = \frac{m_{01}}{m_{00}} \right]$. Last constants are computed using the geometric moments $m_{p,q}^f = \sum_{i=0}^{M-1} \sum_{j=0}^{N-1} f(i, j) (i)^p (j)^q$. Therefore, the JFMs denoted by $|\tilde{\phi}_{n,m}|$ are shift, scale, rotation, and intensity invariant descriptors. As an example, in Fig.(8.3), two types of objects at different positions, sizes, orientations and illumination conditions are shown.

The main objective in invariant classification is to obtain a procedure for selecting discriminative features with small intraclass variance and large interclass separation. In this work is used, a discriminative measure which evaluates the effectiveness of using a feature $|\hat{\phi}_{n,m}|$ to differentiate between C classes of objects. It is defined as,

$$Q_{n,m} = \sum_{c1=1}^{C-1} \sum_{c2=c1-1}^C |\mu_{n,m}^{c1} - \mu_{n,m}^{c2}| - \sum_{c1=1}^C \sigma_{n,m}^{c1}, \quad (8.18)$$

where $\mu_{n,m}^{c1}$ and $\sigma_{n,m}^{c1}$ are the mean and standard deviation of the invariants $|\hat{\phi}_{n,m}^{c1}|$, for the classes of objects to be classified $c1 = 1..C$. The discrimination power of moments

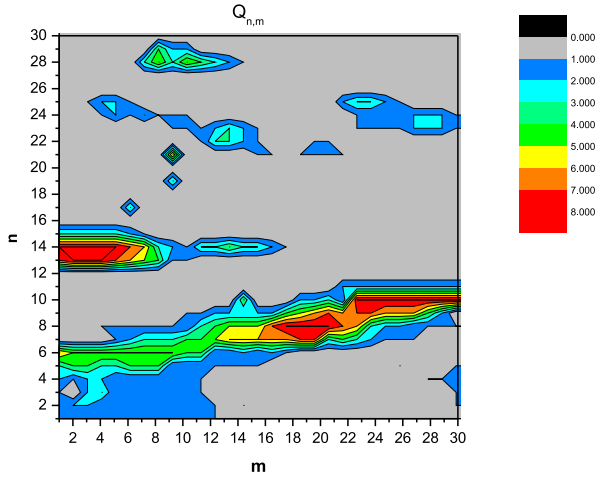


Figure 8.4: Discriminative measure map of invariant moments.

is shown in Fig.(8.4). As it can be seen in the discriminative map, the descriptor $\hat{\phi}_{13,3}$ has a good performance for the set of objects taken from Fig.(8.3).

A feature vector of an object is chosen through the combinations of the best descriptors obtained by the discriminative measure map. The correct rate classification for a set of 120 images of screws is shown in Fig.(8.5). This correct classification rate reaches the 100% for test screw images as shown in Fig.(8.3). As it can be observed the main characteristic of our test images is that they are very similar between themselves. These similarities are related to the millimetric and standard threads. The classification of test images is reached for all the Jacobi-Fourier moment sets even though intensity changes and spatial transformations are done over the input images.

In a second example, some vibration-blurred images are used as test images. A set of this kind of pictures are shown in Fig.(8.6).

It is important taken into account that only one of these images has been chosen for the analysis. It is seen in the graph of Fig.(8.7) that blurring exists in the image and is quantified by a blur radius d . This means that the blurring is minimum at the peaks or at the bottoms of the sine wave vibration, and maximum at the linear part of the graph for the same exposure time interval of the camera sensor. The image blurring can be produced by two kinds of sinusoidal motion, at low or at high frequency. In the first case, the relationship between the time exposition t_e and the period of vibration T_0 is given by $t_e < T_0$, this is called *random motion*. Contrary, when $t_e > T_0$ is called *high frequency motion*.

A graph for the percentage of classification in the particular case of random motion is presented in Fig.(8.8).

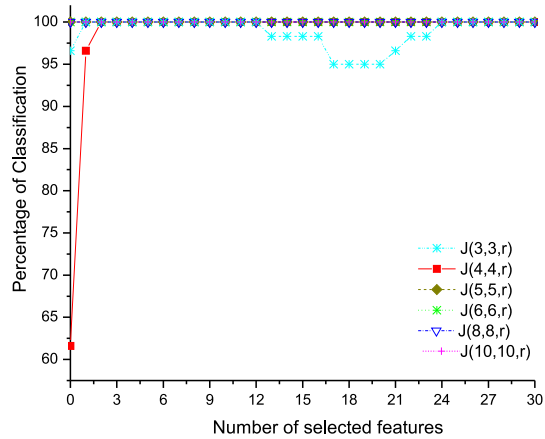


Figure 8.5: Classification percentage using the minimum distance for screw images with variations in scale, intensity, position, and rotation in the input image.

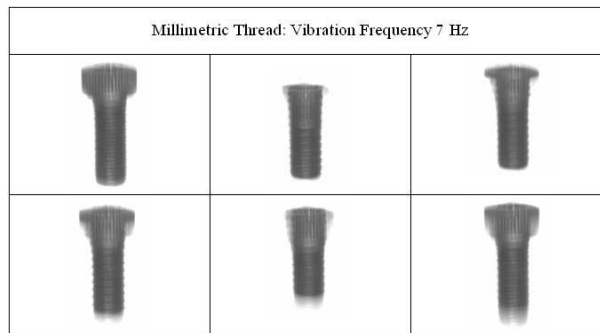


Figure 8.6: Images of screws smeared by vibration. Each frequency increases the blurring in the vertical direction of the image. For the frequency up 7 Hz the blurring does not permit distinguish between the two kinds of thread.

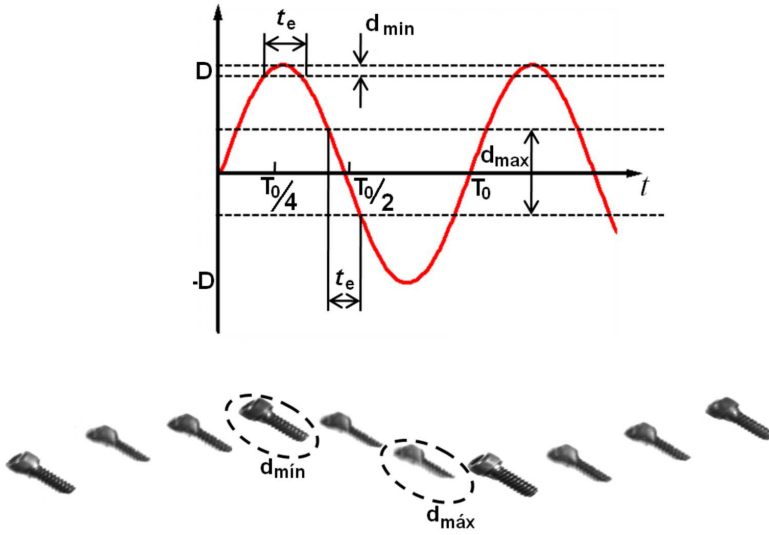


Figure 8.7: Each frequency produces a set of images of the same object. Only one of them is used into the classification method. The blur extension d is obtained at the peaks or at the bottoms of the sine wave vibration function.

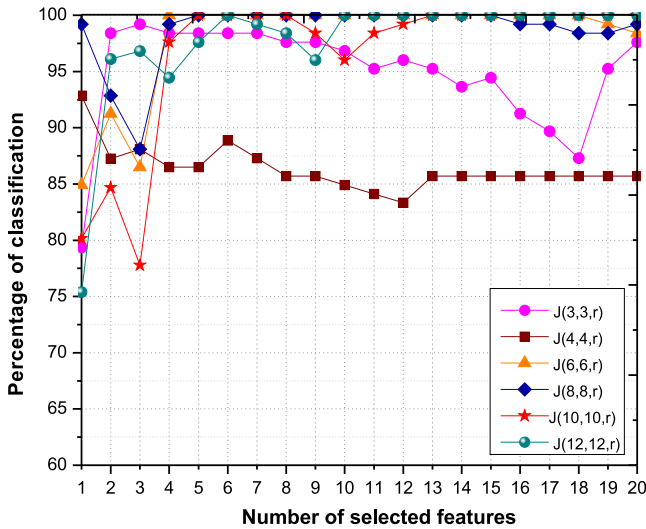


Figure 8.8: Percentage of Classification using the minimum distance, the images of screws are blurred by motion.

8.4 Gait recognition

In the decade of nineties, several algorithms to extract human gait features from image sequences have been studied for individual recognition. They have looked for a specific pattern such as style of walk or pathology. Typically, a model-based approach for human gait is required to estimate certain parameters such as gait frequency, phase, and center of mass coordinates. But this method results in a large number of operations by a single image. Although it is a more accurate model, is also computationally expensive. Other possibilities use holistic measures as Zernike moments [15]. The main advantage is that a holistic method can be computationally cheaper than a model-based approach. A novel holistic method for gait description is based on the Generic Jacobi-Fourier Moment History (JFMH) [10]. Also JFMH can be adapted by a geometrical moment process to generate invariants to translation, illumination, small rotations, and scale of walking people.

The JFMH is defined as a chronological sequence of moments obtained from an image stack. The invariant JFMH is denoted as $\widehat{\phi}_{nm}^{image,serie,person}$ and it is computed as

$$\left| \widehat{\phi}_{nm}^{image,serie,person} \right| = g \left| \sum_{i=0}^{M-1} \sum_{j=0}^{N-1} f_{image}(r_{i,j}, \theta_{i,j}) \widetilde{P}_{nm}(r_{i,j}, \theta_{i,j}) \right| \quad (8.19)$$

where $image = 1 \dots N_I$ are number of images $f_{image}(r_{uv}, \theta_{uv})$, $serie = 1 \dots N_{sr}$ are the index of sequences, $person = 1 \dots N_{prs}$ are the index for the individuals, and g is an intensity factor.

The advantage of using the method of orthogonal moments is in finding the different phases of gait by means of moment histories from frame sequences as shown in Fig.(8.9).

The moments of an image are shape descriptors and the moment history is a temporal function of moments. Figure 8.10 shows plots of particular moment values across two sequences of the same subject. In both cases JFMH profiles are very similar to the same subject but different between subjects.

The starting points of the gait sequences are different. Likewise, the same subject does not walk in the same way in each sample, thus it will be required to chose the better sequences which can be set on phase. A common way to solve this problem is looking for a maximum of the correlation coefficient between a reference section and the overall moment histories by means of Genetic Algorithms (GA).

The procedure consists in choosing an interval of width H of the moment histories $\widehat{\phi}_{nm}^{image,serie,person}$ for each sequence $serie$. The starting point of the selection is given by $Sp(serie)$, where $serie = 1 \dots N_{sr}$. The selected interval of the sequence 1 is shown in Fig.(8.11).

We can propose the *reference* section given by,

$$R_{nm}^{h, person} = \frac{1}{N_{sr}} \sum_{serie=1}^{N_{sr}} \widehat{\phi}_{nm}^{Sp(serie)+h, serie, person} \quad (8.20)$$

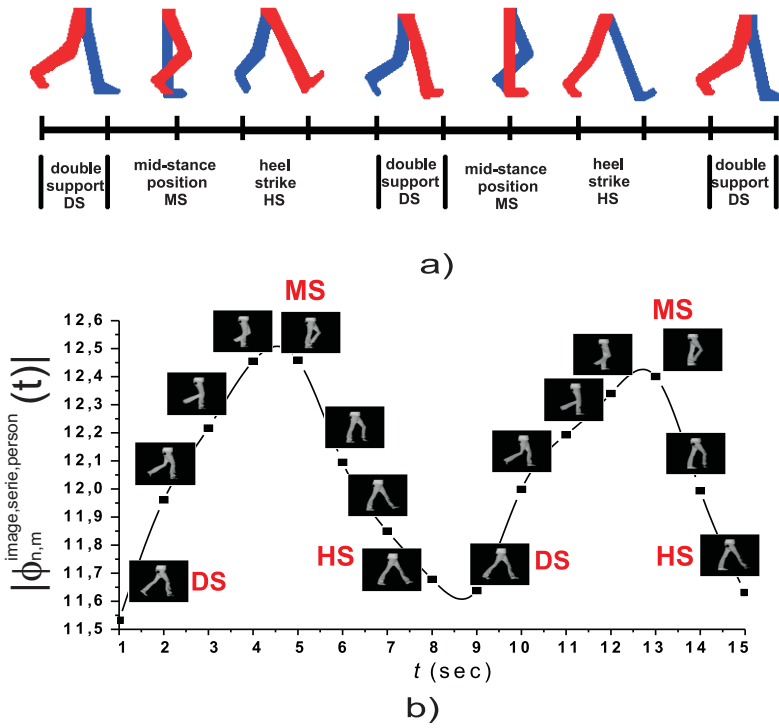


Figure 8.9: Phases of gait by means the JFM history.

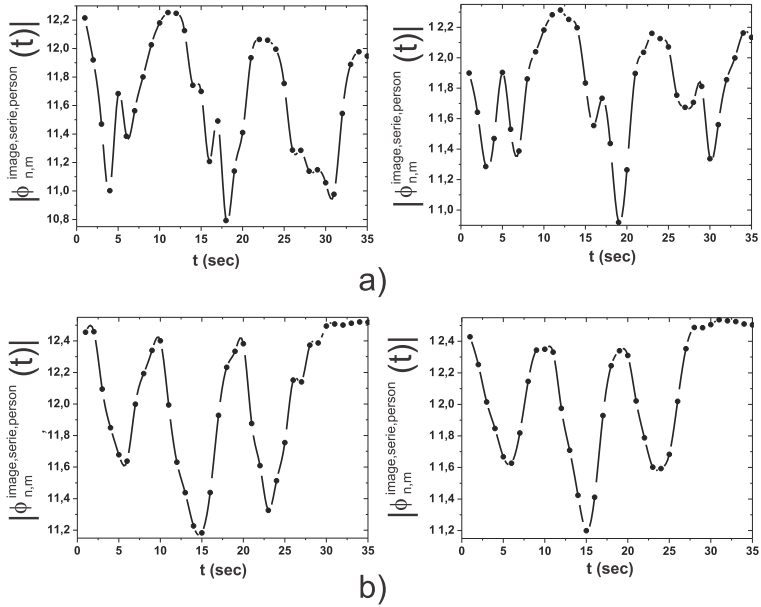


Figure 8.10: Moment history profiles for certain particular values n, m of (a) subject 1 (b) subject 2.

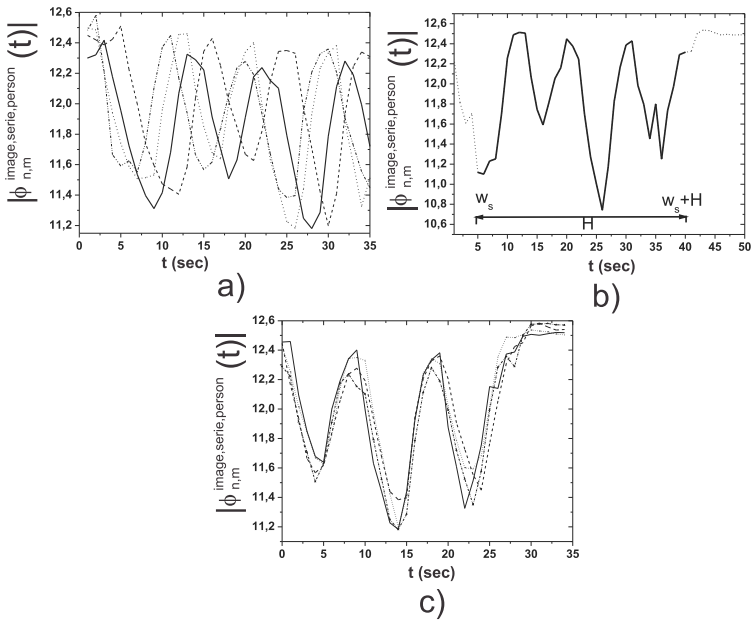


Figure 8.11: Moment histories (a) at any time (b) reference section (c) on phase.

where $h = 1, 2, ..H$.

We are interested in finding intervals of the moment histories which can be correlated with the reference section. If temporal functions of moments can be set on phase, it implies that the subject gait is obtained. Consequently, JFMHs on phase are taken into account as part of the training database.

If we use again the discriminative measure defined before in Eq.(8.18), but to differentiate among C_p persons, it is given by

$$Q_{n,m} = \sum_{c1=1}^{C_p-1} \sum_{c2=c1-1}^{C_p} |\mu_{n,m}^{c1} - \mu_{n,m}^{c2}| - \sum_{c1=1}^{C_p} \sigma_{n,m}^{c1}, \quad (8.21)$$

where $\mu_{n,m}^{c1}$ and $\sigma_{n,m}^{c1}$ are the mean and standard deviation of the phased JFMHs $|\hat{\phi}_{n,m}^{c1}|$.

The best descriptor is found from the discriminative measure Q . Furthermore, the descriptor vector of the person gait is built from the best descriptors. Also it is possible to seek trough Genetic algorithms (GA), an appropriate combination of descriptors. The most effective vector descriptor combines the best descriptors given by the metric Q using GA.

Home database: Our home database consists of 15 subjects walking on a yard under three different distances. The acquisition does not have any control on lighting conditions. Numerical normalization of the silhouette images is achieved by computing the center of mass in the x and y directions, the area, and the intensity of objects using geometric moments. Because of the different distances to the camera, pre-processing silhouettes with sizes of 80×80 , 93×93 and 115×115 pixels are used, some images are shown in Fig.(8.12).

By using the JFMHs with $\alpha = \beta = 10$ to our pre-processing home database the classifications results are shown in Fig.(8.13).

CMU database: In order to carry out the algorithm evaluation another two databases are used. The Carnegie Mellon University Robotics Laboratory (CMU) database is used. It consists of 25 subjects walking on a treadmill. It contains six motion sequences of 11 seconds long, recorded at 30 frames per second. The images have a resolution of 640×480 and were taken under six different viewpoints and two different speeds. Only the normal to the subject walking direction and slow walking speed is analyzed. Some lower body silhouettes from *MoBo* database are shown in Fig.(8.14a). Also scattergrams of 14 shapes of subjects in the $2D$ feature space are shown in Fig.(8.14b). Again, the Jacobi-Fourier descriptors based on $J_n(10, 10, r)$ polynomials achieve a full recognition percentage and the better performance using only ten descriptors. These last results are shown in the curves of the Fig.(8.14c).

Casia A database: The Institute of Automation, Chinese Academy of Sciences (CASIA) provides the CASIA Gait Database to gait recognition and contains three datasets. Our algorithm is tested on DatasetA, this set consists of 20 subjects walking on a yard, and with variation of the walker speed. If the sequences have at least a length of 50 images they are processed. Again, only the normal to the subject walking direction is used. The pre-processing silhouettes from *CASIA_A* database are shown in Fig.(8.15a). Additionally, scattergrams of the 10 shapes of subjects in

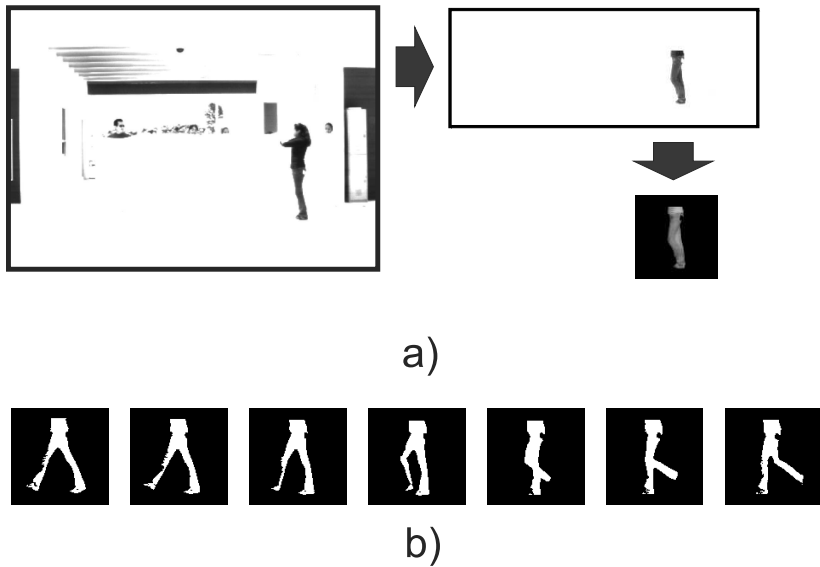


Figure 8.12: (a) Image acquisition process of 15 subjects walking on a yard. (b) Gait cycle sequence of pre-processing images of silhouettes of 93×93 pixels.

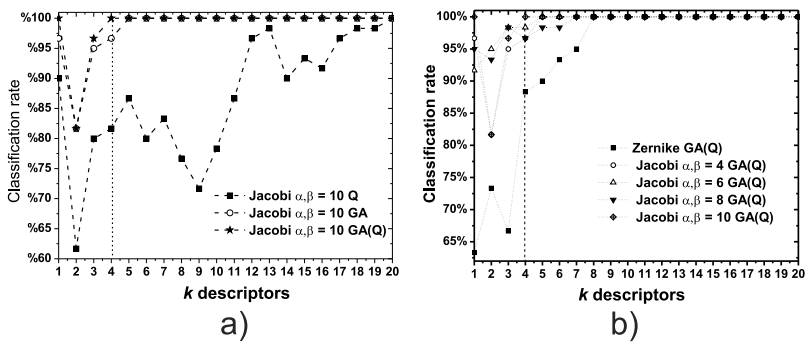


Figure 8.13: CCR of subjects from our home database using a descriptor vector based on JFMs.

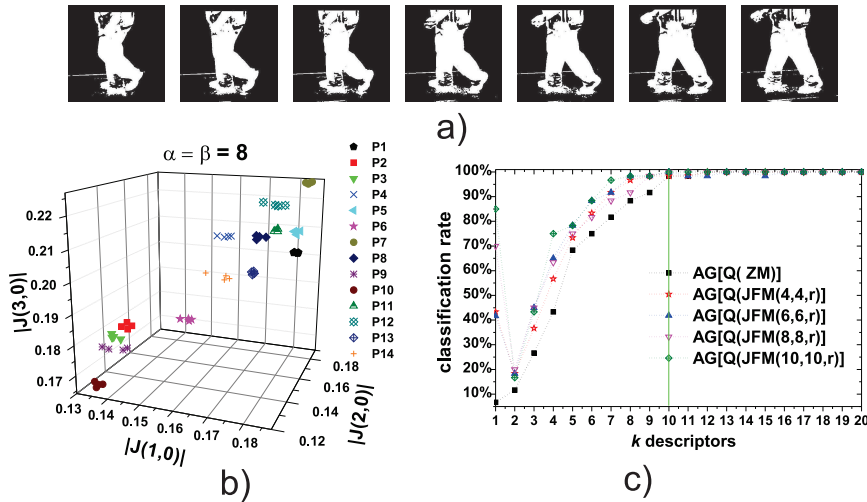


Figure 8.14: (a) Image acquisition of 14 subjects walking on a treadmill, (b) Scattergram, (c) CCR curves.

the 3D feature space are shown in Fig.(8.15b). As in the past examples, Jacobi-Fourier descriptors obtained from $J_n(10,10,r)$ polynomials achieve a full recognition percentage with only three descriptors.

In general, it has been shown that the proposed algorithm has good performance in the three databases, regardless of the different characteristics of each one. Also the indoors and outdoors databases have been used, those with different time intervals, velocities, and distances to the camera. In all cases, only the normal to the subject walking direction is used and just the lower body images are taken into account for computing of moments. The latter means less information and hence less computational effort. Moreover, it can be seen that lower order moments than 9 are required for image description as shown in Fig.(8.15c). In the three databases, six sequences are taken into account as a test subset, two more than the training subset.

8.5 Applications in Image Enhancement

8.5.1 Digital Image Fusion

Image fusion allows merging images from multiple sensors or even multiple images from the same sensor. Its goal is to integrate complementary information to provide a composite image which could be used to better understanding of the entire scene. On the other hand, focusing cameras is an important problem in computer vision and microscopy, due to the limited depth of field of optical lenses in CCD devices. One way to overcome this problem is to take different in-focus parts and combine them into a single composite image which contains the entire focused scene. Many techniques have been used to generate fusion schemes, including Zernike moment function [21].

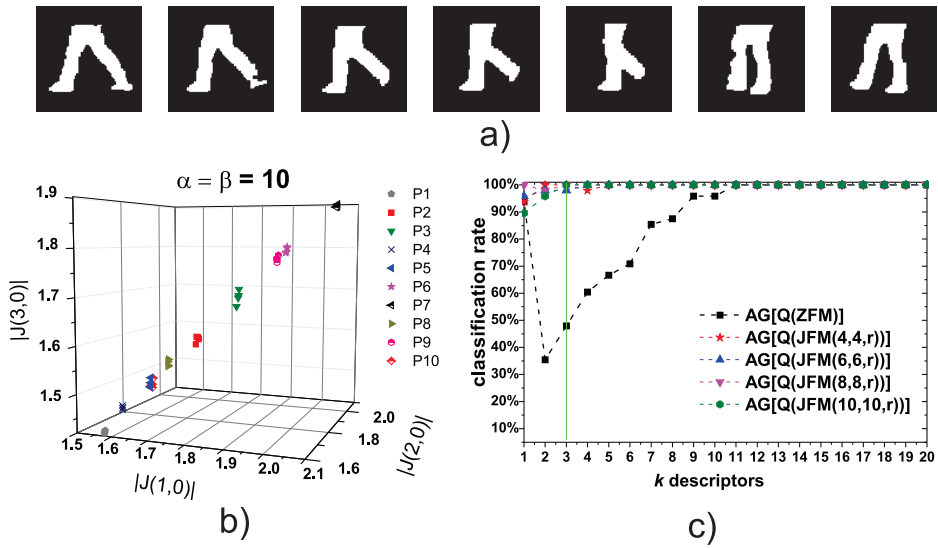


Figure 8.15: (a) Image acquisition of 10 subjects walking on a treadmill, (b) Scattergram, (c) CCR curves.

In this context the fusion of microscope images is done. The procedure is implemented in every channel RGB. The final image fusion results from the input images.

The discrete JFMs $\phi_{n,m}$ are used as a focus measure for evaluating the contrast or sharpness of an image. The contrast measure of a block or region $f^{block}(r_{i,j}, \theta_{i,j})$ in the image is given by,

$$\tilde{\phi}_{n,m}^{block} = \sum_{i=0}^{\Delta x-1} \sum_{j=0}^{\Delta y-1} f^{block}(r_{i,j}, \theta_{i,j}) \tilde{P}_{nm}(r_{i,j}, \theta_{i,j}) \quad (8.22)$$

The input image $f(r, \theta)$ is decomposed into blocks of variable size $\Delta x \times \Delta y$. JFMs are computed for each i th *Block* as a focus measure, and denoted by $\tilde{\phi}_{n,m}^{block}$. From this point, the fused image is constructed by blocks as follows,

$$Block(fused) = \begin{cases} Block(f_1) & \text{if } \left| \tilde{\phi}_{n,m}^{block(f_1)} \right| \geq \left| \tilde{\phi}_{n,m}^{block(f_2)} \right| \\ Block(f_2) & \text{otherwise} \end{cases} \quad (8.23)$$

where $\left| \tilde{\phi}_{n,m}^{block(f_1)} \right|$ denoted the JFMs for the i th *Block*. of an input image $f_1(r, \theta)$.

A fusion scheme based on JFMs is shown in Fig.(8.16).

The test images used in this section are taken by using a microscope optical system with focus at three different planes. Some input images and their JFMs are shown in Fig.(8.17). As we can see, the algorithm identifies focused regions in an input image. The images are fused by comparing the contrast by the method of regions.

Figure 8.18 shows the result on fusing input images using the method of JFMs.

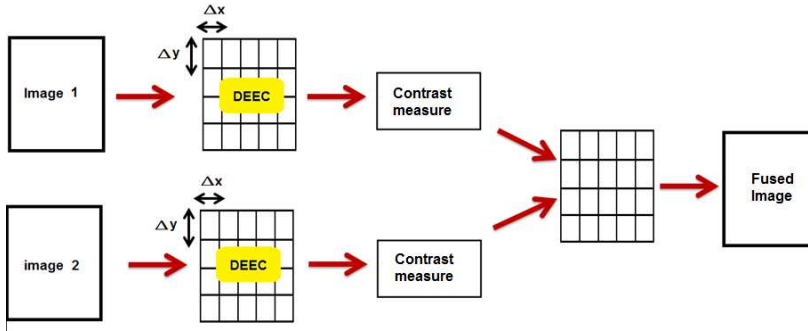


Figure 8.16: Fusion scheme using JFM.

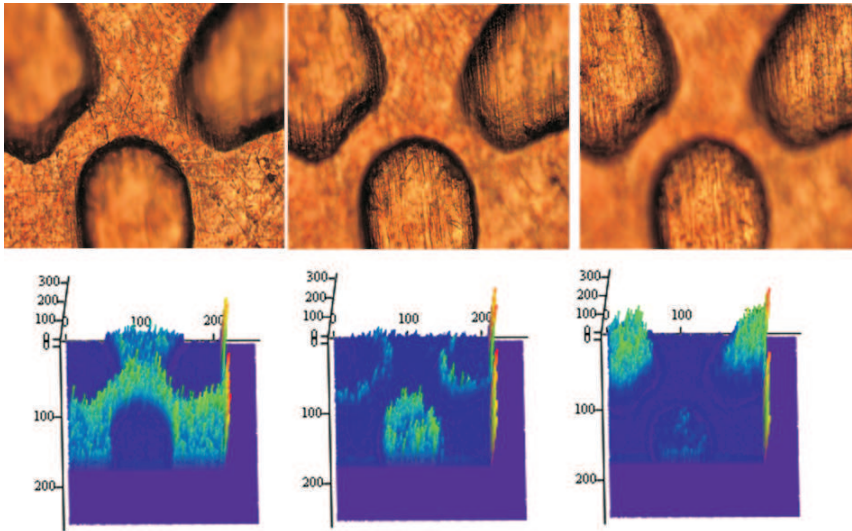


Figure 8.17: Multi-focus input images with three focused regions and their corresponding JFMs. The moments are used as a focus measure for evaluating the contrast or sharpness of a block of region.



Figure 8.18: Result of image fusion of the better focused regions using the maximum value of JFMs from input images.

8.6 High-precision computation of Jacobi-Fourier moments

In the literature, there are few results showing reconstructions of images greater than or equal to 128×128 pixels [19, 16, 22], due to errors inherent in the calculation of moments and high computational times. Recently, it has been demonstrated that the arrangement of polar pixels is fast and has a high-precision in comparison with other methods. In 2007, Xin et al. [23] proposed this approach, which consists in reconfiguring the square pixel array to an arrangement of polar pixels to eliminate errors of geometry and to be able to calculate the integral analytically. Sometime later, Camacho-Bello et al. [5] proposes a recurrence relation to eliminate the numerical instability of the orthogonal polynomials and to compare with other methods in terms of invariance, reconstruction error and computation time.

In a previous analysis, it has been demonstrated, that two types of errors occurred in the direct calculation of orthogonal moments: geometric error and numerical integration error [9]. To increase the numerical accuracy calculation Xin et al. [23] proposed an algorithm based on changing the shape of the square pixels in a polar pixels scheme, as shown in Fig.(8.19). The unit disk of polar pixels scheme is uniformly divided along the radial direction into U sections, with radial distance of $r_u = u/U$ where $u = 1 \dots U$. The number of polar pixels in the u th ring is $S_u = (2u - 1)V$, with angles $\theta_{uv} = (v - 1)2\pi/S_u$, where $v = 1 \dots S_u$ and V is the number of sectors contained in the innermost section. The total number of polar pixels is VU^2 and each of them has an area of π/VU^2 . In practice, Xin et al. [23] recommended to set the value of $V = 4$ and $N/2 \leq U \leq N$ for a $N \times N$ image.

The calculation of the JFMs is performed by summation of all sectors inside the unit disk. Equation 8.1 for the calculation of JFMs are rewritten as

$$\hat{\phi}_{nm} = \sum_{u=1}^U \sum_{v=1}^{(2u-1)V} \hat{f}(r_{uv}, \theta_{uv}) \omega_{nm}(r_{uv}, \theta_{uv}), \quad (8.24)$$

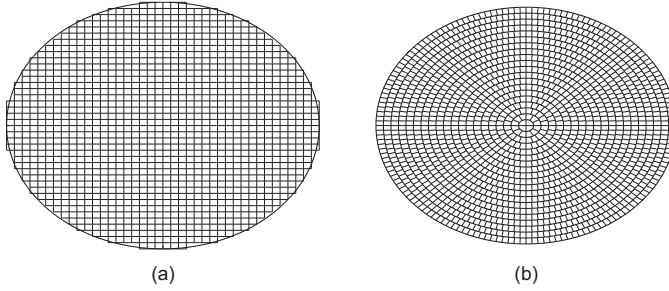


Figure 8.19: Unit disk with a radius of 20 pixels: (a) square pixels, (b) polar pixels.

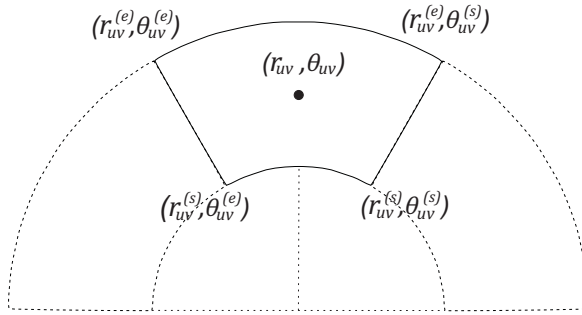


Figure 8.20: Polar pixel representation or concentric sector Ω_{uv} .

where $\hat{f}(r_{uv}, \theta_{uv})$ is an approximation of the function $f(r_{i,j}, \theta_{i,j})$ defined over a set of concentric sectors Ω_{uv} and the factor $\omega_{nm}(r_{uv}, \theta_{uv})$ is given by

$$\begin{aligned} \omega_{nm}(r_{uv}, \theta_{uv}) &= \int \int_{\Omega_{uv}} J_n(\alpha, \beta, r) \exp(jm\theta) r dr d\theta \\ &= \int_{r_{uv}^{(s)}}^{r_{uv}^{(e)}} J_n(\alpha, \beta, r) r dr \int_{\theta_{uv}^{(s)}}^{\theta_{uv}^{(e)}} \exp(jm\theta) d\theta, \quad (8.25) \\ &= I_1 \times I_2 \end{aligned}$$

where $(r_{uv}^{(s)}, \theta_{uv}^{(e)})$, $(r_{uv}^{(s)}, \theta_{uv}^{(s)})$, $(r_{uv}^{(e)}, \theta_{uv}^{(e)})$ and $(r_{uv}^{(e)}, \theta_{uv}^{(s)})$ denote the starting and ending points of the sector Ω_{uv} , where (r_{uv}, θ_{uv}) represent the radius and angle of each sector Ω_{uv} , as shown in Fig.(8.20), respectively. The integral of the complex Fourier component of Eq.(8.25) can be analytically calculated as follows,

$$I_2 = \begin{cases} \frac{j}{m} \left[\exp(-jm\theta_{uv}^{(e)}) - \exp(-jm\theta_{uv}^{(s)}) \right], & m \neq 0 \\ \theta_{uv}^{(e)} - \theta_{uv}^{(s)}, & m = 0 \end{cases}. \quad (8.26)$$

Camacho et al. [5] propose to use 10-point Gaussian quadrature rule with the recurrence relation of Eq.(8.12) for the integral I_1 , which is less accurate but numerically

Table 8.2: Weights (η_k) and location of sampling points (z_k) for 10-point Gaussian quadrature

k	η_k	z_k
1	0.0666713443	-0.9739065285
2	0.1494513492	-0.8650633667
3	0.2190863625	-0.6794095683
4	0.2692667193	-0.4333953941
5	0.2955242247	-0.1488743390
6	0.2955242247	0.1488743390
7	0.2692667193	0.4333953941
8	0.2190863625	0.6794095683
9	0.1494513492	0.8650633667
10	0.0666713443	0.9739065285

more stable for greater than 21 orders. The composite Gaussian quadrature rule for numerical integration of the Jacobi polynomial can be stated as,

$$I_1 = \frac{r_{uv}^{(e)} - r_{uv}^{(s)}}{2} \sum_{k=1}^{10} \eta_k J_n \left(\alpha, \beta, \frac{r_{uv}^{(e)} - r_{uv}^{(s)}}{2} z_k + \frac{r_{uv}^{(e)} + r_{uv}^{(s)}}{2} \right). \quad (8.27)$$

where η_k are weights and $z_k \in [-1, 1]$ are the points where the function is evaluated. The values of η_k and z_k are given in Table 8.2.

The locations of the Cartesian pixels do not coincide with those of the polar pixels, as shown in Fig.(8.19). This problem can be resolved by bicubic interpolation of third order introduced in reference [8]. Cubic convolution interpolation is a new technique for resampling discrete data. The cubic convolution interpolation kernel is given by

$$u(x) = \begin{cases} \frac{3}{2}|x|^3 - \frac{5}{2}|x|^2 + 1 & 0 < |x| < 1 \\ -\frac{1}{2}|x|^3 + \frac{5}{2}|x|^2 - 4|x| + 2 & 1 < |x| < 2 \\ 0 & 2 < |x| \end{cases}. \quad (8.28)$$

The image value at Ω_{uv} can be estimated via the two-dimensional cubic convolution interpolation function, this function is expressed by

$$\hat{f}(r_{uv}, \theta_{uv}) = \sum_{i=k-1}^{k+2} \sum_{j=l-1}^{l+2} f(i, j) u(k-i) u(l-j) \quad (8.29)$$

where u is the interpolation kernel of Eq.(8.28) and $k = \frac{N}{2} r_{uv} \cos \theta_{uv} + \frac{N}{2} + 1$, and $l = \frac{N}{2} r_{uv} \sin \theta_{uv} + \frac{N}{2} + 1$. Figure 8.21 shows the Lena image of 64×64 pixels and its representation in polar pixels with parameters $V = 4$ and $U = 32$. The polar pixel values were obtained by bicubic interpolation of Eq.(8.29).



Figure 8.21: Lena image: (a) square pixels, (b) polar pixels.

8.7 Image Reconstruction

Image reconstruction can help to determine how well an image can be characterized by a small finite set of its moments. According to orthogonal theories, an original image $f(i, j)$ can be reconstructed by an infinite number of JFMs. The reconstructed discrete distribution of the image is given by

$$\tilde{f}(i, j) = \sum_{n=0}^L \sum_{m=0}^L \left| \hat{\phi}_{nm} \right| J_n(\alpha, \beta, r_{ij}) \exp(-jm\theta_{ij}) \quad (8.30)$$

where $\tilde{f}(i, j)$ is the reconstructed version of $f(i, j)$, and L is the maximum order of JFMs used in the reconstruction of the image. The *NIRE* is used for the performance analysis of orthogonal moments [14]. It is defined as the normalized mean square error between the input image $f(i, j)$ and its reconstruction $\tilde{f}(i, j)$, in discrete form is given by,

$$NIRE = \frac{\sum_{i=0}^{N-1} \sum_{j=0}^{M-1} \left[\tilde{f}(i, j) - f(i, j) \right]^2}{\sum_{i=0}^{N-1} \sum_{j=0}^{M-1} f^2(i, j)}. \quad (8.31)$$

Bhatia and Wolf pointed out [3] there is an infinite number of complete sets of orthogonal polynomials that are invariant to rotation and can be obtained from the Jacobi polynomials. Each set is obtained by the combination of the parameters α and β . Therefore, there may be a set of orthogonal moments better fit to specific applications. The fast calculation of the JFMs facilitates the search for the best values α and β that best fit specific applications. Camacho et al. [5] define the mean of *NIRE* as metric to quantitatively evaluate the best combinations of α and β . The mean value of *NIRE* is given by,

$$\Psi(\alpha, \beta, p) = \frac{1}{p} \sum_{L=1}^p NIRE(L, \alpha, \beta), \quad (8.32)$$

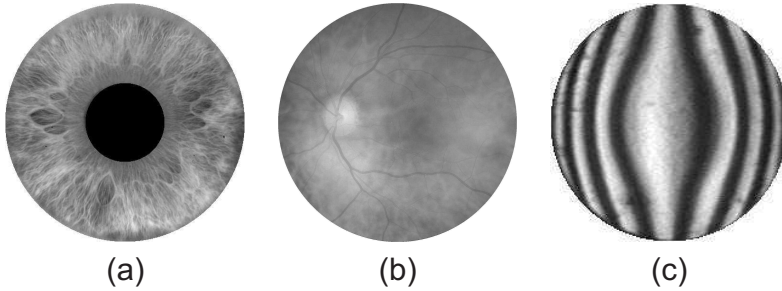


Figure 8.22: Test images: (a) iris of a human eye, (b) cornea of a human eye, (c) ronchigram.

where L is the maximum order of JFMs used in the reconstruction of the input image and p is the cutting orders.

In this section a comparative analysis is performed, in terms of the reconstruction error for different values of α and β for images of radial symmetry. This kind of images may have some interesting applications such as iris recognition, retina inspection and analysis of ronchigrams [11], as shown in Fig.(8.22). We conducted an exhaustive search of the $\alpha = 1 \dots 10$ and $\beta = 1 \dots 10$ values in order to find the optimal combination of parameters α and β that best reconstruct the test images. The results of the three test images are presented below.

Iris image: The graph of Fig.(8.23a) shows the results of Eq.(8.32), which present local minima using the following relationship $\alpha = 2\beta - 2$. Here the Pseudo-Jacobi-Fourier moments satisfy this condition. The minimum value of the search neighborhood is when $\alpha = 10$ and $\beta = 6$. The NIRE for the minimum value and some nearby values are shown in Fig.(8.23b). Also, the reconstruction with the best parameters $\alpha = 10$ and $\beta = 6$ is shown in Fig.(8.23c).

Cornea Image: The results of the search neighborhood are shown in Fig.(8.24a), as can be seen the minimum values are found when $\alpha = \beta$; the Mellin-Fourier and shifted Legendre-Fourier moments satisfy this condition. Newly, the results of NIRE when $\alpha = \beta = 1, 2, 3, 4, 5$ are shown in Fig.(8.24b). Finally, the image reconstruction of the cornea when $\alpha = \beta = 1$ are shown in Fig.(8.24c), these last found values have the best performance.

Ronchigram Image: In Fig.(8.25a) is shown that the minimum values for the average of the NIRE is found when $\alpha = \beta$. The NIRE for the highest values are shown in Fig.(8.25b), as can be seen these values have better performance when $\alpha = \beta = 2$. Also, the reconstruction of these values is shown in Fig.(8.25c).

The results of the search for the best parameters α and β for the test images have particular behavior, the zero values of $\alpha - \beta$ are related to the minimum values of the search space. For example, images of the ronchigram and cornea have better performance when $\alpha - \beta = 0$ and the worst results when $\alpha - \beta = 9$. Therefore, the greater difference of $\alpha - \beta$, the greater the average of NIRE. In the iris image, the pupil area has values of zero, for this reason the minimum of the search neighborhood are displaced by the expression $|\alpha - 2\beta - 2|$. Also note that, the results of Figures

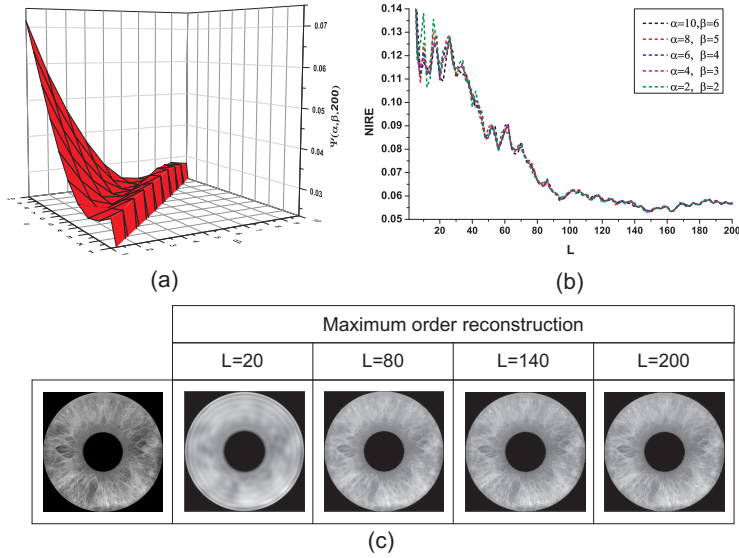


Figure 8.23: Results of the iris image. (a) Chart for finding the best values α and β . (b) NIRE of the best parameters. (c) Reconstruction of iris image with $\alpha = 10$ and $\beta = 8$.

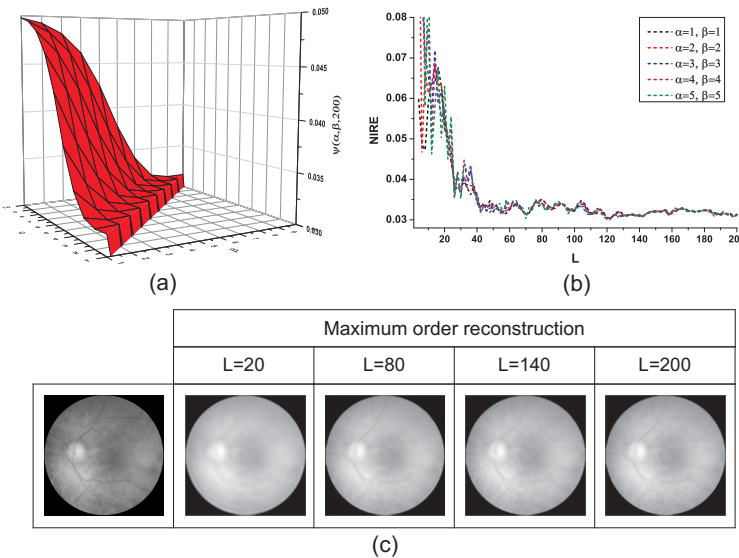


Figure 8.24: Results of the cornea image. (a) Chart for finding the best values α and β . (b) NIRE of the best parameters. (c) Reconstruction of cornea image with $\alpha = \beta = 1$.

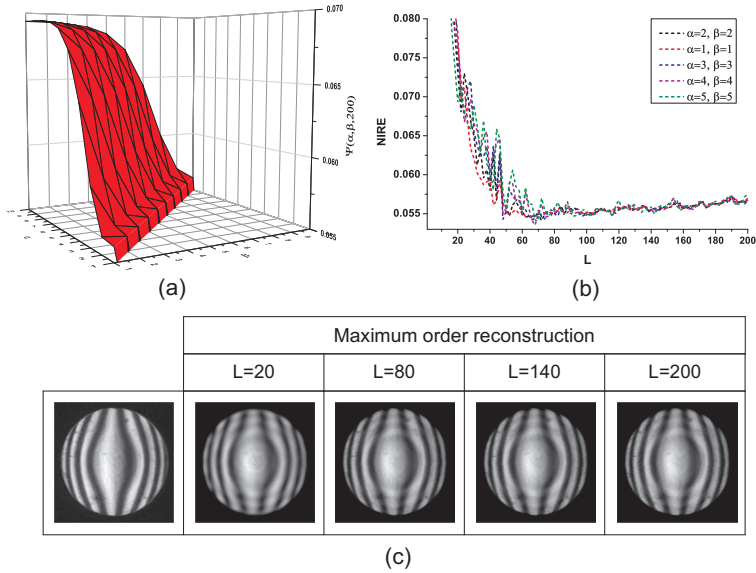


Figure 8.25: Results of the ronchigram image. (a) Chart for finding the best values α and β . (b) NIRE of the best parameters. (c) Reconstruction of ronchigram image with $\alpha = \beta = 2$.

8.23b, 8.24b and 8.25b, do not undergo significant changes in NIRE for the minimum values that were found.

8.8 Conclusions

The method of Generic orthogonal moments based on the Jacobi-Fourier polynomials has been presented. Because the moment invariants are useful feature descriptors for pattern recognition, we have investigated them and proven for gait description from sequences of lower body images. One of the main contributions of this method is the temporal correlation of JFM Histories using genetic algorithms. Also, the different phases of gait are obtained by means the JFMHs in a sequence. Three gait databases are used for algorithm evaluation: our home database, MoBo, and CASIA A. The starting point of the gait cycles is solved through Genetic Algorithms. It is known that, the kernel of the moments based on the Generic Jacobi functions generates an infinity number of orthogonal polynomial families. For this reason, a graphical analysis is done to determine the parameter values for α and β which should be bounded in the interval $[0, 1]$. Besides, JFM are adapted by a geometrical moment procedure to generate invariants to translation, illumination, small rotations, and scale of walking people. During the analysis, two discriminative maps are obtained. The so-called Q discriminative measure and the $GA(Q)$ evolved discriminative map.

Another application of the Jacobi-Fourier moments have been used to classify mechanical parts blurred by motion. The classification method is applied to images of

screws with millimetric and standard thread, with little differences between them. The motion blurred images are acquired under high frequency sinusoidal motion. Temporal functions can be obtained following the centroid of mass of the object using geometric moments. With the level of distortion in the images produced by the vibration experiments, the Jacobi-Fourier moments are capable to discriminate between the two classes of objects until some level of blurring, using a few Jacobi-Fourier descriptors as is shown.

Besides in digital image enhancement, a new algorithm for multi-focus image fusion has been proposed. The focus measure is based in orthogonal Generic moments of a discrete image function. The algorithm divides the input images into blocks and evaluate the contrast of each block. From this point of view, the boundaries between focused and defocused regions can be determined. The method selects the better focused regions to create the final focused image. The fusion of microscope images proposed here is illustrated for the case of color images defined in the RGB space. The results show that, the method based on Jacobi-Fourier moments can produce a fused image with better contrast that the corresponding defocused regions, even more the original hue is conserved.

Also, we have proposed a novel approach for high-precision, fast computation of JFMs. Furthermore, this approach allows us to generate sets of different orthogonal moments. The arrangement of polar pixels used and the proposed recurrence relationships for different polynomial families improves computation time and reconstruction error for gray-level images with large size. The numerical stability and accuracy of our method is proved through the NIRE. Therefore, the proposed method is not only faster, but is also high precision and numerically stable. It has direct applications in pattern recognition problems where invariant feature vectors are needed.

Finally, we have reconstructed gray-level images such as the Iris, Retina and Ronchigrams images using the Jacobi-Fourier moment sets. The performance of these moments in image reconstruction has been measured by only one image quality metrics such as the NIRE. As it has been shown the contrast in the reconstructed images has been practically retrieved in overall way.

References

- [1] M. Abramowitz and I.A. Stegun. *Handbook of Functions With Formulas, Graphs and Mathematical Tables*. Dover, New York, 1964.
- [2] G. Amu, S. Hasi, X. Yang, and Z. Ping. Image analysis by Pseudo-Jacobi ($p = 4$, $q = 3$)-Fourier moments. *Applied Optics*, 43:2093–2101, 2004.
- [3] A.B. Bhatia and E. Wolf. On the circle polynomials of Zernike and related orthogonal sets. In *Mathematical Proceedings of the Cambridge Philosophical Society*, volume 50, 1954.
- [4] B. Buchner and P. O’Leary. Real-time stereo for industrial inspection. In *Machine Vision Applications in Industrial Inspection XII*, volume 5303 of *SPIE*, 2004.
- [5] C. Camacho-Bello, C. Toxqui-Quitl, A. Padilla-Vivanco, and J. Báez-Rojas. High-precision and fast computation of Jacobi-Fourier moments for image description. *J. Opt. Soc. Am.*, 31(1):124–134, 2014.

- [6] P. Geveaux, S. Kohler, J. Miteran, F. Truchetet, and F. Meriaudeau. Comparison between two classification methods: application to defects detection by artificial vision in industrial field. In *Machine Vision Applications in Industrial Inspection VIII*, volume 3966 of *SPIE*, pages 154–161, 2000.
- [7] T.V. Hoang and S. Tabbone. Errata and comments on generic orthogonal moments: Jacobi-Fourier moments for invariant image description. *Pattern Recognition*, 46(11):3148–3155, 2013.
- [8] R. Keys. Cubic convolution interpolation for digital image processing. *IEEE Transactions on Acoustics, Speech and Signal Processing*, 29(6):1153–1160, 1981.
- [9] S.X. Liao and M. Pawlak. On the accuracy of Zernike moments for image analysis. *IEEE Transactions on Pattern Analysis and Machine Intelligence*, 20(12):1358–1364, 1998.
- [10] A. Padilla-Vivanco. Gait recognition by Jacobi-Fourier moments. In *Frontiers in Optics 2011/Laser Science XXVII, OSA Technical Digest*, page paper JTUA19, 2011.
- [11] A. Padilla-Vivanco, G. Urcid-Serrano, F. Granados-Agustín, and A. Cornejo-Rodríguez. Comparative analysis of pattern reconstruction using orthogonal moments. *Optical Engineering*, 46(1):017002, 2007.
- [12] Z. Ping, H. Ren, J. Zou, Y. Sheng, and W. Bo. Generic orthogonal moments: Jacobi-Fourier moments for invariant image description. *Pattern Recognition*, 40(4):1245–1254, 2007.
- [13] Z. Ping, R. Wu, and Y. Sheng. Image description with Chebyshev-Fourier moments. *J. Opt. Soc. Am.*, 19:1748–1754, 2002.
- [14] Y. Sheng and L. Shen. Orthogonal Fourier-Mellin moments for invariant pattern recognition. *J. Opt. Soc. Am.*, 11(6):1748–1757, 1994.
- [15] J.D. Shutler and M.S. Nixon. Zernike velocity moments for sequence-based description of moving features. *Image and Vision Computing*, 24(4):343–356, 2006.
- [16] C. Singh, Ekta Walia, and Rahul Upneja. Accurate calculation of Zernike moments. *Information Sciences*, 233:255–275, 2013.
- [17] M.R. Teague. Image analysis via the general theory of moments. *J. Opt. Soc. Am.*, 70(8):920–930, 1980.
- [18] C.H. Teh and R.T. Chin. On image analysis by the methods of moments. *IEEE Transactions on Pattern Analysis and Machine Intelligence*, 10(4):496–513, 1988.
- [19] C. Toxqui-Quitl, L. Gutiérrez-Lazcano, A. Padilla-Vivanco, and C. Camacho-Bello. Gray-level image reconstruction using Bessel-Fourier moments. In *22nd Congress of the International Commission for Optics: Light for the Development of the World*, volume 8011 of *SPIE*, page 80112T, 2011.
- [20] C. Toxqui-Quitl, A. Padilla-Vivanco, and C. Santiago Tepantlán. Minimum image resolution for shape recognition using the generic Jacobi Fourier moments. In *22nd Congress of the International Commission for Optics: Light for the Development of the World*, volume 8011 of *SPIE*, page 80117W, 2011.
- [21] C. Toxqui-Quitl, E. Velázquez-Ramírez, A. Padilla-Vivanco, J. Solís-Villarreal, and C. Santiago-Tepantlán. Multifocus image fusion using Zernike moments. In *Applications of Digital Image Processing XXXV*, volume 8499 of *SPIE*, page 849921, 2012.
- [22] E. Walia, C. Singh, and A. Goyal. On the fast computation of orthogonal Fourier-

- Mellin moments with improved numerical stability. *Journal of Real-Time Image Processing*, 7(4):247–256, 2012.
- [23] Y. Xin, M. Pawlak, and S. Liao. Accurate computation of Zernike moments in polar coordinates. *IEEE Transactions on Image Processing*, 16(2):581–587, 2007.